An Integrated Dual-Band Dual-Circularly Polarized Shared-Aperture Transmit-Array Antenna for K-/Ka-Band Applications Enabled by Polarization Twisting Elements

Xuanfeng Tong, Zhi Hao Jiang, Yuan Li, Fan Wu, Jianjun Wu, Ronan Sauleau, Wei Hong

An Integrated Dual-Band Dual-Circularly-Polarized Shared-Aperture Transmit-Array Antenna for *K*-/*Ka*-Band Applications Enabled by Polarization Twisting Elements

Xuanfeng Tong, *Graduate Student Member*, *IEEE*, Zhi Hao Jiang, *Member*, *IEEE*, Yuan Li, *Graduate Student Member*, *IEEE*, Fan Wu, *Member*, *IEEE*, Jianjun Wu, Ronan Sauleau, *Fellow*, *IEEE*, and Wei Hong, *Fellow*, *IEEE*

***Abstract*—An integrated dual-band dual-circularly-polarized (dual-CP) transmit-array (TA) antenna operating at *K*- and *Ka*-bands is proposed. Antenna-filter-antenna based polarization twisting TA cells possessing high cross-polarized and low co-polarized linearly-polarized transmission characteristics are designed. These TA cells possess highly-efficient circular-polarization transmission with flipped handedness without using any 180° phase shifting lines, thus bringing about benefits such as symmetrical structures, design simplification, and more consistent CP transmission magnitudes. In addition, the dual-band dual-CP transmissive beamforming characteristics are realized by arranging *K*- and *Ka*-band cells in the same aperture and employing hybrid phase compensation strategy. For reducing the overall device profile, right-handed CP (RHCP) and left-handed CP (LHCP) planar arrays operating at *K*- and *Ka*-bands are fabricated as feeds for the TA. A dual-band dual-CP TA antenna with independently controllable beam directions is synthesized and experimentally demonstrated. The measured 2-dB gain and axial ratio bandwidths are 11.7% and 10.2% for *K*-band RHCP and LHCP beams, and the two CP beams own bandwidths of about 7.5% at *Ka*-band. The proposed dual-band dual-CP TA antenna can be a promising candidate for satellite communications and so on.**

***Index Terms*—Dual-band, dual-circularly-polarization, millimeter-wave, transmit-arrays, shared-aperture.**

Manuscript received July 6, 2022. This work was supported in part by National Natural Science Foundation of China (NSFC) under Grants 62122019, 62293492, and 61901106, and in part by the ZTE Corporation and the State Key Laboratory of Mobile Network and Mobile Multimedia Technology, and in part by The Major Key Project of PCL (PCL2021A01-2). (*Corresponding author: Zhi Hao Jiang.*)

X. Tong and Y. Li are with the State Key Laboratory of Millimeter Waves, School of Information Science and Engineering, Southeast University, Nanjing 210096, China.

Z. H. Jiang, F. Wu, and W. Hong are with the State Key Laboratory of Millimeter Waves, School of Information Science and Engineering, Southeast University, Nanjing 210096, China (e-mail: zhihao.jiang@seu.edu.cn).

J. Wu is with the State Key Laboratory of Mobile Network and Mobile Multimedia Technology, ZTE Corporation, Shanghai 201203, China.

R. Sauleau is with Univ Rennes, 1CNRS, IETR - UMR 6164, F-35000 Rennes, France.

I. Introduction

SATELLITE communication has been playing an increasingly important role over the past a few decades, which will be served as an indispensable part of the 6th-generation (6G) wireless network that provides unified space-air-ground interconnections [1]. For the purpose of improving overall payload efficiency and increasing system capacity density, antennas with multi-beam and multi-color reuse characteristics are highly desirable for high throughput satellites (HTS) [2], [3]. For four-color reuse scheme, the conventional solution requires four reflector antennas assembled on the same satellite with a single-feed-per-beam configuration [4]. In order to reduce the number of apertures and achieve planar structures, transmit-arrays (TAs) generating high-gain beams of dual-frequency and dual-polarization can provide a promising solution for HTS applications and so on [5].

Dual-band TAs share a similar working principle with single-band TAs, with a difference manifested by the fact that the phase compensation at each of the two bands should be able to be manipulated independently. So far, dual-band linearly-polarized (LP) and circularly-polarized (CP) shared-aperture TAs have been proposed by employing antenna-filter-antenna (AFA) cells [6]–[9] and multi-layered phased shifting surfaces (PSSs) building blocks [10]–[15]. By utilizing LP patch radiators as the receiving elements and the same LP patches with Berry phase (BP) determined variable rotation angles placed on the transmitting side for both bands, a dual-band CP TA antenna is proposed [7]. It possesses a 3-dB gain and axial ratio (AR) < 3 dB bandwidth of around 7% at both bands. A dual-band CP TA antenna is presented by employing multi-layered PSSs [13], which exhibits a 3-dB gain and AR bandwidth of 10% and 7% at the low-band and high-band, respectively.

For the purpose of increasing the spectral efficiency of communication systems, TAs with dual-polarized characteristics have been widely explored in recent years [16]–[22]. In [18], a dual-LP TA antenna is realized by placing rectangular patches on both sides of a ground plane etched out with cross-shaped slots. The beam directions for the orthogonal

polarizations can be independently controlled by modifying the sizes of the rectangular patches and cross-shaped slots for each polarization, offering a 3-dB gain bandwidth of about 18% for the dual-LP beams. In contrast to dual-LP TAs, dual-CP TAs are more desirable for space applications, which are more difficult to be designed [21], [22]. By combining a bottom dual-LP TA composed by +45° and +135° polarized AFA cells and a top LP-to-CP polarizer, a TA antenna with dual-CP feature is achieved [21], [23]. This dual-CP TA antenna owns a bandwidth of about 7.3% with gain variation and AR below 3 dB for both CP beams. For the purpose of reducing the panel thickness of dual-CP TAs, more recently, single-functional-layer designs have been proposed by jointly exploiting dynamic phase (DP) and Berry phase (BP) compensation techniques [22], [24]. Such dual-CP TA possesses a joint 2-dB gain and AR < 2 dB bandwidth of about 12.3% for both CP beams [22].

Dual-band or dual-polarized antennas can support two-color reuse scheme for satellite communication applications [25]. In contrast, antennas with simultaneous dual-band and dual-polarization characteristics compatible with four-color reuse strategy can further improve the spectral efficiency particularly for high throughput applications [3]. Recently, dual-band dual-CP reflect-array (RA) antennas have been actively investigated and reported [26]–[29]. In order to eliminate the feed blockage of RA antennas, dual-band and dual-polarized TA antennas are studied. For example, shared-aperture metallic slots [30] or loop elements [31] have been utilized for achieving dual-band dual-LP TAs. However, the LP characteristics of these dual-band dual-LP TAs requires exact alignment between the transmitter and receiver, thereby restricting their practical applications [30], [31]. Therefore, it is urgent to design TA antennas possessing dual-band dual-CP radiation features with four independently controllable beams, which are amenable for a variety of space applications.

In this paper, an integrated dual-band dual-CP TA antenna is reported for generating two *K*-band beams and two *Ka*-band beams with independently controllable beamforming. By taking advantage of the high cross-polarized and low co-polarized LP transmission features, the designed polarization twisting cells, which provide a high CP transmission with handedness flip characteristics, possess symmetrical structure, reduced design complexity, and more stable CP transmission magnitudes. Moreover, by jointly employing shared-aperture cell alignment, hybrid DP and BP compensation strategy, and planar wideband CP feeds, the desirable functionality with a reduced total profile and a high efficiency of the TA antenna is realized. The paper is organized as follows. In Section II, the configuration of the integrated TA antenna, the mathematical derivation of the transmission matrix of the transmissive dual-CP cells, as well as the scheme and performances of the dual-band dual-CP TA cells are illustrated. *K*- and *Ka*-band RHCP and LHCP planar arrays, acting as the feeds, are reported in Section III. The experimental results of the TA antenna, integrated with the planar feeds, are presented in Section III. Finally, the conclusion is drawn in Section IV.

II. TA Configuration and Design of Dual-Band Dual-CP Shared-Aperture TA Cells

Fig. 1 depicts the diagram of the integrated dual-band dual-CP TA antenna, which comprises a feed array and a quasi-circular planar TA. The feeds are composed of *K*-/*Ka*-band RHCP/LHCP four-element planar arrays, which are placed underneath the TA at a focal distance of *F*. The generated *K*-/*Ka*-band RHCP beams are directed at $(\theta_R, \varphi_R)_{K/Ka}$ when the *K*-/*Ka*-band LHCP waves emitted from feed is illuminated on the TA, whereas the TA can radiate *K*-/*Ka*-band LHCP waves pointing at $(\theta_L, \varphi_L)_{K/Ka}$ by exciting the *K*-/*Ka*-band RHCP feeds, respectively. The directions of the four generated beams can be manipulated independently. In addition, the top-right inset of Fig. 1 illustrates the directions of the four beams of the proof-of-concept TA design demonstarted in this work.

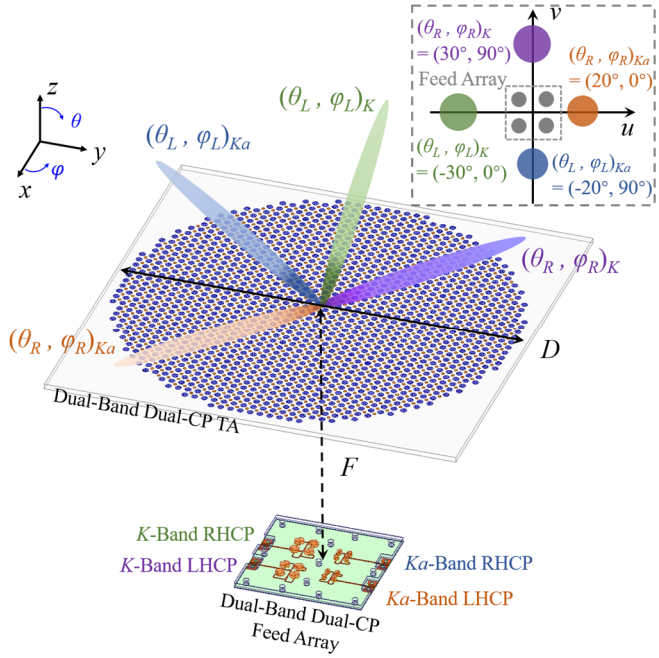

Fig. 1. Configuration of the integrated dual-band dual-CP TA antenna. The beam directions and feed array positions are presented in the top-right inset, where the subscripts *R*/*L* denotes the abbreviation of the RHCP/LHCP waves.

A. Transmission Coefficient Matrix Derivation

For a true dual-CP cell, the transmission phases, for example, the $\phi(t_{RL})$ and $\phi(t_{LR})$, should be able to be controlled independently. One of the approaches to achieve dual-CP beamforming is designing a series of cells possessing the following three characteristics. First, the co-polarized LP transmission magnitudes (T_{xx} and T_{yy}) should be close to zero. Second, the cross-polarized LP transmission magnitudes (T_{xy} and T_{yx}) need to be near unity. Third, the cross-polarized LP transmission phases ($\phi(t_{xy})$ and $\phi(t_{yx})$) can provide a full 360° coverage and are identical to each other. This indicates that highly-transmissive polarization twisting cells with variable transmission phases are desirable. As such, the linear transmission matrix of these cells can be written as

$$\begin{bmatrix} t_{xx} & t_{xy} \\ t_{yx} & t_{yy} \end{bmatrix} = \begin{bmatrix} 0 & e^{j\phi_n} \\ e^{j\phi_n} & 0 \end{bmatrix}, \quad (1)$$

where the subscript *n* represents the cell number with *n* = *m*+1,

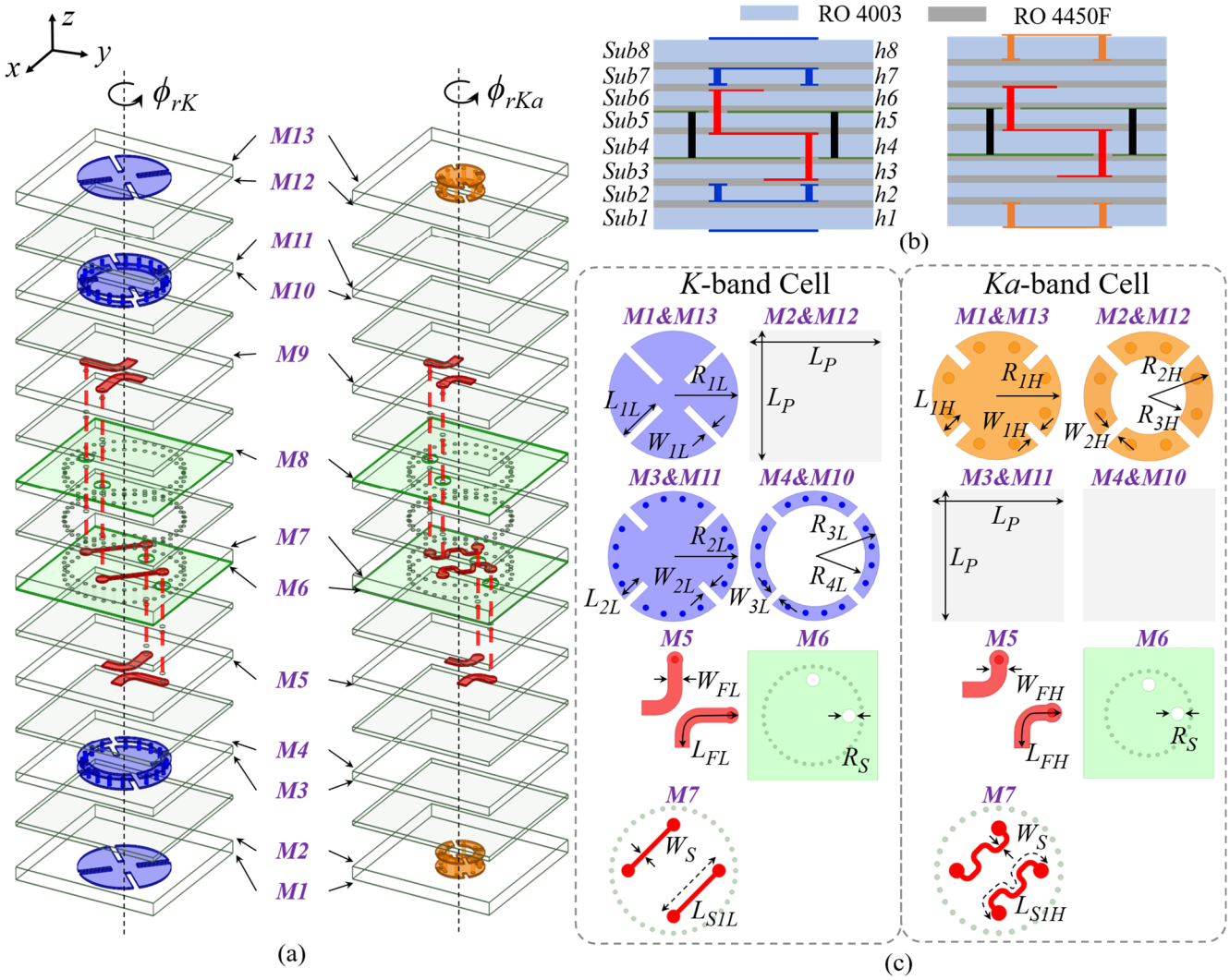

Fig. 2. (a) Configurations of the TA elements. (b) The laminated structure of the TA elements, where *h1* = 0.305, *h2* = 0.203, *h3* = 0.203, *h4* = 0.305, *h5* = 0.203, *h6* = 0.203, *h7* = 0.203, and *h8* = 0.305. The relative permittivity and loss tangent are 3.55 and 0.0027 for Rogers 4003, and 3.52 and 0.004 for Rogers 4450F, respectively. (c) Top views of the metallic layers (the *M8* and *M9* layers are not shown here, due to they can be achieved by rotating the *M6* and *M5* layers with an angle of 180°), where L_P = 5.4, R_{1L} = 1.6, L_{1L} = 1.15, W_{1L} = 0.2, R_{2L} = 1.6, L_{2L} = 0.65, W_{2L} = 0.2, R_{3L} = 1.6, R_{4L} = 1.25, W_{3L} = 0.2, W_{FL} = 0.4, L_{FL} = 2.2, R_S = 0.56, W_S = 0.15, R_{1H} = 0.85, L_{1H} = 0.3, W_{1H} = 0.15, R_{2H} = 0.85, R_{3H} = 0.5, W_{2H} = 0.15, W_{FH} = 0.35, and L_{FH} = 1.5, all in millimeters.

under the condition that the resolution of the dual-CP cells is $m \times m$ bit. The CP transmission matrix can then be obtained as [32], [33]

$$\begin{bmatrix} t_{RR} & t_{RL} \\ t_{LR} & t_{LL} \end{bmatrix} = \begin{bmatrix} 0 & e^{j(\phi_n - 2\phi_r - \frac{\pi}{2})} \\ e^{j(\phi_n + 2\phi_r + \frac{\pi}{2})} & 0 \end{bmatrix}. \quad (2)$$

It can be concluded from (2) that the LHCP (RHCP) incident waves are all transformed into the RHCP (LHCP) transmissive waves after passing through the dual-CP cells. In addition, such a cell is capable of separately controlling the cross-polarized CP transmission phases by rotating the cells with a different initial cross-polarized LP transmission phase, indicating that the CP waves with opposite handedness can be manipulated separately.

Although both the dual-CP cells designed in this work and those reported in [22] possess a single functional layer, it should be underlined that they operate based on different mechanism. First, the TA cells with high cross-polarized and low co-polarized LP transmission can inherently enable high CP transmission with handedness flip. Secondly, symmetrical structure would be achieved due to the elimination of the $\lambda_g/2$ length difference between the phase shifting lines in the cells, resulting in reduced design complexity and smaller cell footprint. Thirdly, the designed cells would possess more consistent and stable transmission magnitudes for CP waves with opposite handedness than dual-CP TA cells using phase shifting lines with an 180° phase difference, which would facilitate a balanced behavior for the transmitted LHCP and RHCP beams [see Eq. (2)]. In theory, the operating bandwidth of the designed cells could be made to be very broad since they do not rely on dispersive phase shifting lines with an 180° difference. Therefore, the operational bandwidth of the designed dual-CP cells is primarily dependent on the impedance matching bandwidth of the utilized receiving and transmitting radiators.

B. 2 × 2 Bit Dual-CP Phase Compensating TA Cell Designs

TA cells can be realized based on AFA structures [6–9, 16–18, 21–22], multi-layered PSSs [10–15, 19], and metamaterials [34, 35]. In this design, the AFA structure is adopted for designing the TA cells due to its inherent low panel thickness. Fig. 2(a) shows the configurations of the designed elements at the two operational bands, both having eight Rogers 4003 substrates that are bonded together using seven Rogers 4450F prepregs with a thickness of 0.1 mm. The total thickness of the TA panel is 2.77 mm, i.e., about $0.18\lambda_K$, where λ_K is the free-space wavelength at 19.5 GHz [see Fig. 2(b)]. The receiving and transmitting radiators of the *K*-band and *Ka*-band elements are composed of dual-LP L-probe fed stacked patches and single patch, respectively, as shown in Fig. 2(a). For size miniaturization, the L-probes (*M5* and *M9* layers) are bent into opposite directions, while four rectangular slots are etched on the all the patches. In addition, the *K*-band lower patch and *Ka*-band patch are bent inward using metallic vias for further miniaturization [36]. By back-to-back placing the receiving and transmitting radiators and electrically connecting them through two striplines of the same lengths (see *M7* layer), *K*- and *Ka*-band polarization twisting TA elements are formed [see Fig. 2(a) and (c)].

For the purpose of compensating the phases of the spherical waves emitted from feed, two kinds of phase delay techniques can be utilized, i.e., DP and BP [33]. When DP compensation is adopted, a series of cells with variable sizes or variable delay line lengths covering a full phase period of 360° need to be designed. In this way, if the RHCP or LHCP waves emitted from feed illuminate on the TA aperture, the transmitted CP waves keep the same polarization as the incident waves for cells without any phase difference between their two optical axes. In contrast, the transmitted CP wave will have a handedness opposite to that of the incident CP wave if the TA cells behave as transmissive half-wave plates. However, both the transmitted LHCP and RHCP waves will point to the same direction since only DP compensation is used [13], [33]. Different from the DP method, the BP compensation approach provides a phase modulation inherently for CP waves by rotating the TA cells behaving as transmissive half-wave plates [33], [37]. The transmitted RHCP/LHCP waves undergo opposite phase gradients when passing through the TA aperture, i.e., the beam directions are symmetrical about the aperture normal for the orthogonal CP waves. Specifically, when the incident RHCP (LHCP) wave is illuminated on the TA composed by BP cells, the transmitted wave is transformed into an LHCP (RHCP) beam [38], [39]. As such, it is impossible to manipulate the orthogonal CP waves independently by only adopting the DP or BP method. However, when DP and BP are simultaneously applied to the TA cells, the dual-CP waves can be controlled separately [22]. Therefore, four *K*-band elements and four *Ka*-band elements are designed with a phase gradient of 45°, which can cover a phase range of 180°. In addition, by rotating the cells by an angle of 90°, a full phase period can be obtained at both the *K*- and *Ka*-bands [27]. Finally, by introducing element rotation induced BP delays, dual-band dual-CP phase compensation can be achieved.

As deduced above, in order to independently control the CP waves with opposite handedness, a hybrid DP and BP compensation method needs to be exploited for the TA cells. The designed polarization twisting TA cells should characterize high cross-polarized and low co-polarized LP transmission magnitudes, as well as the same transmission phases for the cross-polarized LP waves according to Eq. (1). Therefore, the designed dual-LP L-probe fed patch radiators are adopted and placed back-to-back on both the receiving and transmitting sides, which are connected through two striplines to form the polarization twisting TA elements as shown in Fig. 2(a). In addition, a series of metal vias connecting the top and bottom ground planes with a diameter of 0.15 mm are added for suppressing the parallel-plate waveguide mode [40]. In particular, the *x*-polarized (*y*-polarized) port of the receiving radiator is connected to the *y*-polarized (*x*-polarized) port of the transmitting radiator through a stripline, offering a high cross-polarized and a low co-polarized LP transmission. Two striplines functioning as phase delay lines possess the same length for each TA element, providing the same cross-polarized LP transmission phases. This also leads to a reduced design complexity as well as a smaller element footprint. Fig. 3(a) and (d) show the trace patterns of the phase delay lines with different lengths for obtaining a gradient cross-polarized LP transmission phase of 45° at each band, i.e., a 3-bit LP phase resolution. It should be noted that the designed TA elements can be viewed as transmissive half-wave plates with optical axes along the ±45°. By interlacing the *K*- and *Ka*-band elements with an element spacing of 5.4 mm, corresponding to $0.35\lambda_K$ ($0.53\lambda_{Ka}$), true dual-band dual-CP TA cells can be constructed.

The simulated co-polarized and cross-polarized LP transmission magnitudes as well as the cross-polarized LP transmission phases are shown in Fig. 3(b) and (e), respectively. From 18.4 to 20.5 GHz and 28.7 to 31.6 GHz, the cross-polarized LP transmission magnitudes are above -2 dB, while the co-polarized LP transmission magnitudes are smaller than -10.7 dB and -16.7 dB for all the cells within the two bands. The cross-polarized LP transmission phases show a phase difference of about 45° between the four cells at both bands. The LP and CP scattering parameters can be transformed to each other [32]. In the range of 18.4 – 20.5 GHz and 28.7 – 31.6 GHz, the cross-polarized CP transmission magnitudes are higher than -2 dB, whereas the co-polarized magnitudes are lower than -10.7 dB and -16.7 dB as presented in Fig. 3(c) and (f). The cross-polarized CP transmission bandwidths are corresponding to the impedance matched bandwidth of the receiving and transmitting radiators, which corroborates the theoretical predictions on the relationship between the operational bandwidth of the TA cells and the impedance bandwidth of the receiving/transmitting radiators. In addition, the dual-CP cells designed in this work show more consistent CP transmission magnitudes between T_{RL} and T_{LR} (T_{RR} and T_{LL}) due to their symmetrical geometrical structures, resulting in a balanced behavior for the transmitted LHCP and RHCP waves.

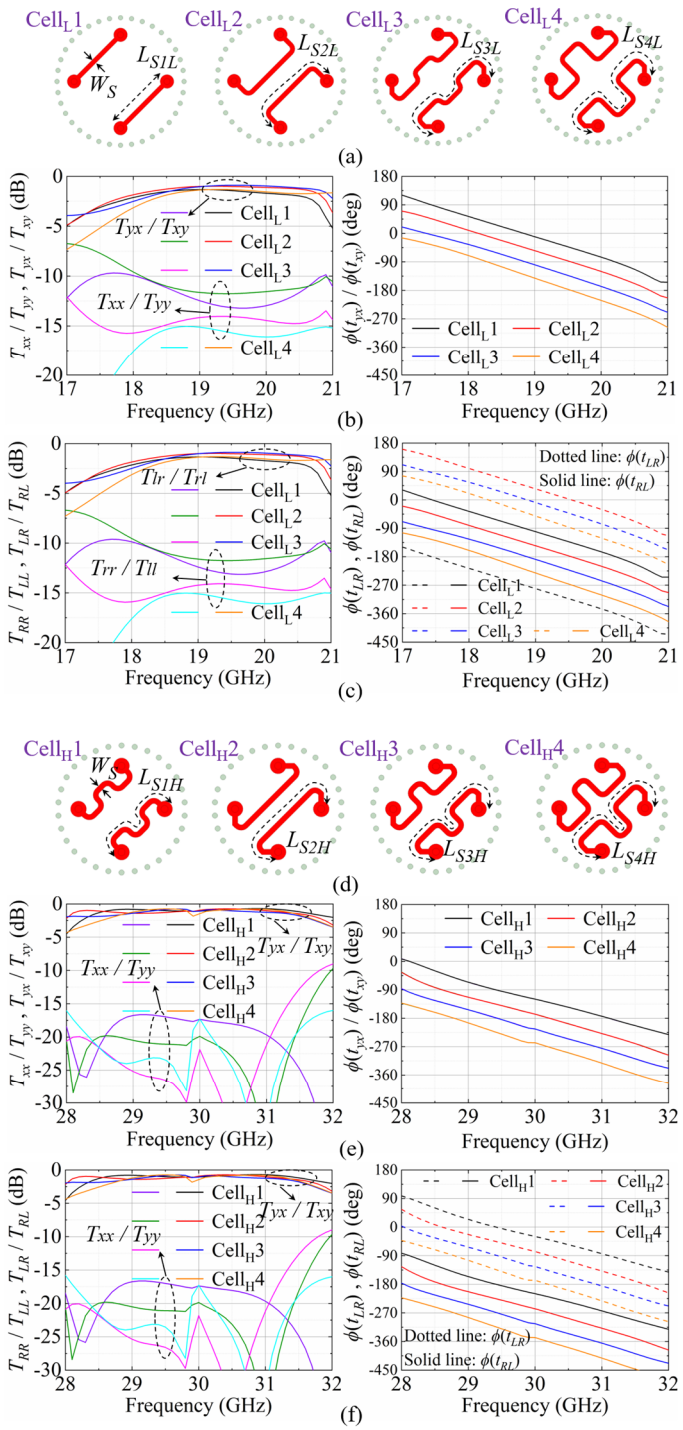

Fig. 3. Top views of the phase-delay striplines (*M7* layer) of the (a) four *K*-band elements and (d) four *Ka*-band elements, with L_{S1L} = 2.12, L_{S2L} = 3.43, L_{S3L} = 4.98, L_{S4L} = 6.14, and L_{S1H} = 2.86, L_{S2H} = 3.74, L_{S3H} = 4.86, L_{S4H} = 5.44, all in millimeters. Simulated LP scattering properties of the (b) four *K*-band cells and (e) four *Ka*-band cells. Simulated CP scattering properties of the (c) four *K*-band cells and (f) four *Ka*-band cells.

Since the 3-bit LP elements are designed at both bands, respectively, dual-CP phase compensation can be achieved by introducing a proper amount of rotation for each element [22]. As a result, the relationships between the element number, rotation angles, and 2-bit cross-polarized CP transmission phases are provided in Table I. A total of 32 cells, i.e., 16 for *K*-band and 16 for *Ka*-band operation, are simulated using the high-frequency structure simulator (HFSS). The interstellar plots of the simulated cross-polarized CP transmission magnitudes and phases at 19.5 GHz and 29.5 GHz are shown in Fig. 4. The cross-polarized transmission magnitudes are in the range of -1.5 – -0.7 dB for all the 32 cells [see Fig. 4(a) and (c)]. Besides, the cross-polarized CP transmission phases for all the cells are provided in Fig. 4(b) and (d), showing a 2 × 2 bit dual-CP phase compensation with a maximum phase error of 10° and 6.5° at *K*- and *Ka*-bands, respectively.

TABLE I. 2 × 2 BIT DUAL-BAND DUAL-CP PHASE COMPENSATION

$\phi(t_{LR})$ \ $\phi(t_{RL})$	0°	-90°	-180°	-270°
0°	**Cell11*** (Cell3, 45°)	**Cell12** (Cell4, 22.5°)	**Cell13** (Cell1, 90°)	**Cell14** (Cell2, 67.5°)
-90°	**Cell21** (Cell4, 67.5°)	**Cell22** (Cell1, 135°)	**Cell23** (Cell2, 112.5°)	**Cell24** (Cell3, 90°)
-180°	**Cell31** (Cell1, 0°)	**Cell32** (Cell2, 157.5°)	**Cell33** (Cell3, 135°)	**Cell34** (Cell4, 112.5°)
-270°	**Cell41** (Cell2, 22.5°)	**Cell42** (Cell3, 0°)	**Cell43** (Cell4, 157.5°)	**Cell44** (Cell1, 45°)

* The bold font represents the element number of the proposed 16 elements at *K*-band or *Ka*-band. The first word in the bracket indicates the number of the four *K*-/*Ka*-band elements, while the second word in the bracket denotes the rotation angles, i.e., ϕ_{rK} or ϕ_{rKa} [see Fig.2].

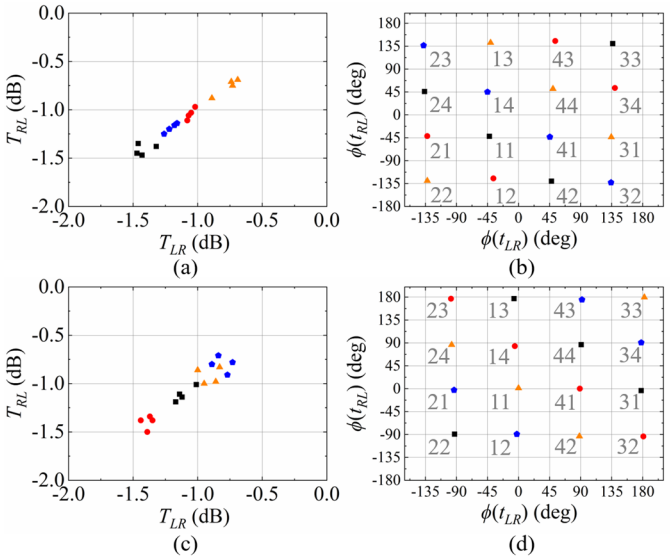

Fig. 4. Interstellar plots of the simulated (a) cross-polarized CP transmission magnitudes and (b) phases for the 16 dual-CP cells at *K*-band. Interstellar plots of the simulated (c) cross-polarized CP transmission magnitudes and (d) phases for the 16 dual-CP cells at *Ka*-band.

C. Interaction Between the K- and Ka-Band Elements

For a shared-aperture TA, the designed *K*- and *Ka*-band 2 × 2 bit dual-CP elements are spatially interleaved. Therefore, it is necessary to study the interaction between the adjacent elements in different frequency bands by observing the inter-band influence on the CP scattering parameters. For simplicity, considering two specific cases where the *K*-band $Cell_L34$ (and $Cell_L44$) is located at the center surrounded by *Ka*-band $Cell_H1$ (and $Cell_H2$). As the *Ka*-band element rotates around its own geometrical center from 0° to 157.5° at an interval of 22.5°, the CP scattering parameters of *K*-band elements are shown in Fig. 5. It can be seen that the discrepancy of the co-polarized and cross-polarized CP transmission magnitudes are smaller than

0.14 dB and 0.6 dB, while the change of the cross-polarized CP transmission phase is less than 5.5°. In contrast, for the cases where the $Cell_H11$ (and $Cell_H23$) is located at the center surrounded by the $Cell_L2$ (and $Cell_L4$). It can be seen that, as the *K*-band element rotates, the cross-polarized CP transmission magnitudes vary between -0.8 and -1.5 dB, while the co-polarized transmission magnitudes are all below -14.4 dB for *Ka*-band elements [see Fig. 5]. The cross-polarized CP transmission phase experiences a small change of less than 8°. It can be concluded from the above discussion that the inter-band interaction between the two bands is negligible, which will not deteriorate the property of the shared-aperture TA antenna.

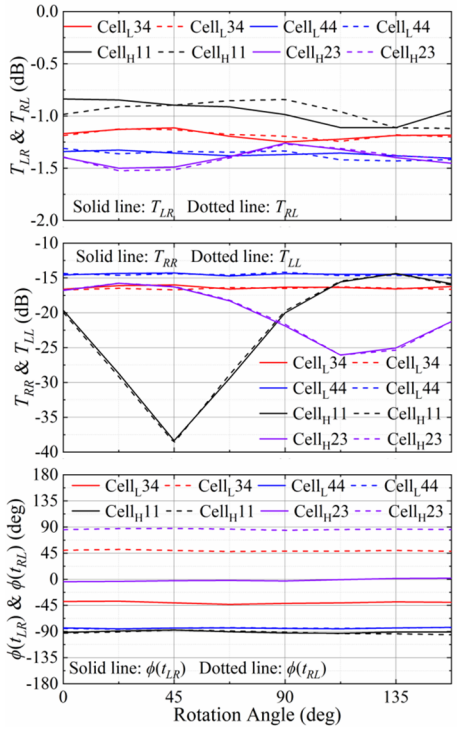

Fig. 5. Simulated CP scattering properties of TA elements ($Cell_L34$, $Cell_L44$) surrounded by rotating element ($Cell_H1$, $Cell_H2$), and TA elements ($Cell_H11$, $Cell_H23$) surrounded by rotating element ($Cell_L2$, $Cell_L4$).

D. Performance of the TA Cells at Oblique Incidence

In general, the performance of the TA cells is different at normal and oblique angles of incidence. Therefore, it is essential to evaluate the cell performance at oblique incidence since the edge cells in the TA aperture are inevitably illuminate by obliquely impinging waves. Here, two TA cells, which contain $Cell_L31$ and $Cell_H12$, and $Cell_L43$ and $Cell_H12$, respectively, are taken to investigate the *K*-band oblique incidence performance. It can be seen that the T_{RL} and T_{LR} are between -1.5 dB and -0.7 dB, and the change of $\phi(t_{RL})$ and $\phi(t_{LR})$ is smaller than 18.1° for both $Cell_L31$ and $Cell_L43$ when the incident angle increase from 0° to 40° [see Fig. 6]. Meanwhile, the co-polarized CP transmission magnitudes are lower than -13 dB and -16 dB for $Cell_L31$ and $Cell_L43$, respectively, for all the incident angles as presented in Fig. 6. Similarly, two TA cells composed of $Cell_H14$ and $Cell_L43$, and $Cell_H24$ and $Cell_L43$ are taken to evaluate the *Ka*-band oblique incidence performance. The fluctuation of the cross-polarized CP transmission magnitudes and phases are smaller 0.5 dB and 29.6° for both $Cell_H14$ and $Cell_H24$, when the incident angle increase from 0° to 40° [see Fig. 6]. In addition, the co-polarized CP transmission magnitudes under incident angle from 0° to 40° are lower than -14.7 dB and -15.4 dB for $Cell_H14$ and $Cell_H24$, respectively. Benefiting from the small element spacing, the TA cell performance keep stable even when the incident angle increases to 40° at both *K*- and *Ka*-bands. The well-behaved cell performance can ensure a smaller focal-to-diameter (*F*/*D*) values, indicating a lower overall profile of the TA antenna.

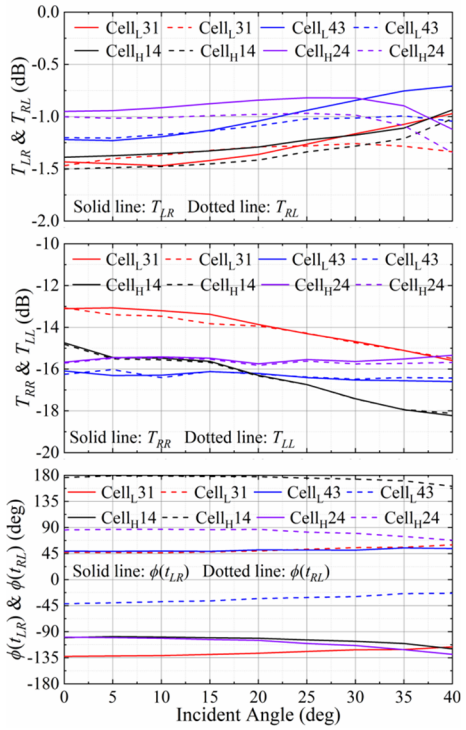

Fig. 6. Simulated CP scattering properties for TA cells as a function of incident angles of $Cell_L31$, $Cell_L43$ at 19.5 GHz, and $Cell_H14$, $Cell_H24$ at 29.5 GHz.

III. Designs and Experimental Verifications of the Dual-Band Dual-CP TA Antenna

With the designed dual-band 2 × 2 bit dual-CP TA cells, a proof-of-concept finite-sized TA antenna is synthesized for further verifying the performance of the proposed TA cells. In addition, planar CP arrays instead of bulky CP horns are designed and utilized as the feeding sources.

A. Planar CP Feed Array Designs

In order to reduce the overall profile of the final TA antenna, planar feeds are preferable for better integration and easy connection with other front-end RF circuits. Here, RHCP/LHCP planar arrays operating at *K*- and *Ka*-bands are designed and used as the feeds [see Fig. 7]. The feed array is composed of three substrates, which include a Rogers 4003 layer (h_{f1} = 0.305 mm) at the bottom, a TLY-5 substrate (h_{f2} = 0.76 mm) in the middle, and a TLY-5 laminate (h_{f3} = 0.25 mm) on the top. Between the bottom and middle substrates, a 0.1 mm-thick Rogers 4450F prepreg is used for bonding purpose. In addition, an air spacer with a thickness of h_{fa} = 1.5 mm is used between the middle and top substrates for separating the

stacked patches. The radiating elements are four circular stacked patches, aligned in a sequential rotation fashion, each with a pair of rectangular shaped notches [see Fig. 7(b) and (c)]. The stacked patches are excited by a microstrip feeding circuit through I-shaped slots on the ground. Since the substrate stackings are the same for the *K*- and *Ka*-bands RHCP/LHCP arrays, they can be readily incorporated in the same multi-layered substrate for high integration.

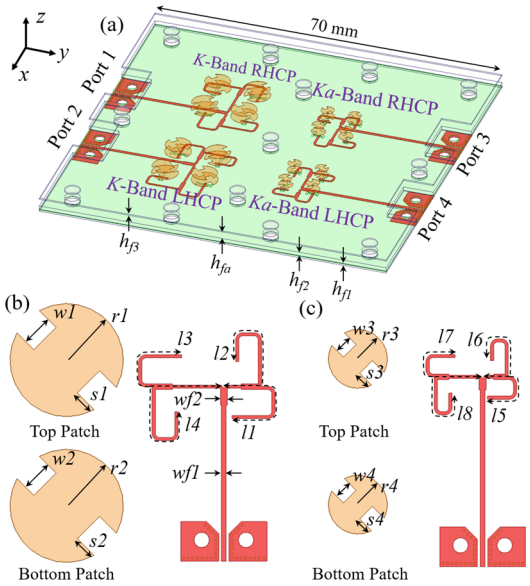

Fig. 7. (a) Configurations of the planar *K*- and *Ka*-band RHCP/LHCP feed arrays. The relative permittivity and loss tangent are 2.2 and 0.0009 for TLY-5 substrate. Top views of the (b) *K*-band and (c) *Ka*-band stacked patches and microstrip feeding circuits with $r1 = 2.6$, $w1 = 1.3$, $s1 = 1.25$, $r2 = 2.5$, $w2 = 1.4$, $s2 = 1.15$, $wf1 = 0.41$, $wf2 = 0.75$, $l1 = 14.74$, $l2 = 17.33$, $l3 = 19.22$, $l4 = 21.81$, $r3 = 1.4$, $w3 = 0.6$, $s3 = 0.95$, $r4 = 1.3$, $w4 = 0.8$, $s4 = 0.8$, $l5 = 9.4$, $l6 = 11.73$, $l7 = 12.4$, and $l8 = 14.73$, all in millimeters.

The *K*- and *Ka*-band planar RHCP/LHCP arrays are simulated, fabricated, and characterized. The measured reflection and mutual coupling coefficients are shown in Fig. 8. The measured reflection coefficients are all smaller than -14 dB in their operational bands, while the mutual couplings between different ports are all lower than -22 dB. The radiation property of the planar CP arrays is measured with the results reported in Figs. 9 and 10. The normalized radiation CP patterns of the *K*-band RHCP and LHCP arrays in simulation and measurement at 19.5 GHz are shown in Fig. 9(a) and (b). It can be seen that the -10 dB beamwidth is around 86° in both planes. The simulated and measured normalized radiation patterns for the CP beams at 29.5 GHz are also provided [see Fig. 9(c) and (d)]. The -10 dB beamwidth is around 85° in both planes for the two arrays. The peak gain and AR values as a function of frequency of the *K*- and *Ka*-band RHCP/LHCP arrays in simulation and measurement are shown in Fig. 10. Both the RHCP and LHCP arrays operating at *K*-band exhibit a moderate measured averaged peak gain of around 9.7 dBic with AR values below 2 dB in the frequency range of 18 – 21.9 GHz. For the *Ka*-band arrays, the measured averaged peak gain is around 9.6 dBic between 27.2 and 31.1 GHz, while the measured AR values are below 3 dB within this band. The discrepancies between the simulated and measured results are mainly attributed to the variation of the air spacer thickness caused during the assembly process. It can be seen from the simulations and measurements that the designed *K*- and *Ka*-band CP planar arrays can be qualified candidates as the feeds of TAs due to their wide impedance bandwidth, moderate -10 dB beamwidth, stable peak gain, and low AR values.

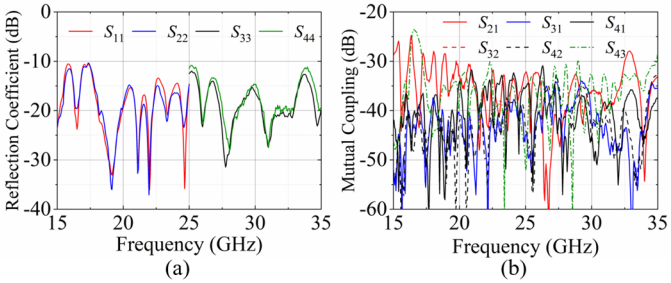

Fig. 8. Measured (a) reflection coefficients and (b) mutual couplings of the *K*- and *Ka*-band planar RHCP/LHCP arrays.

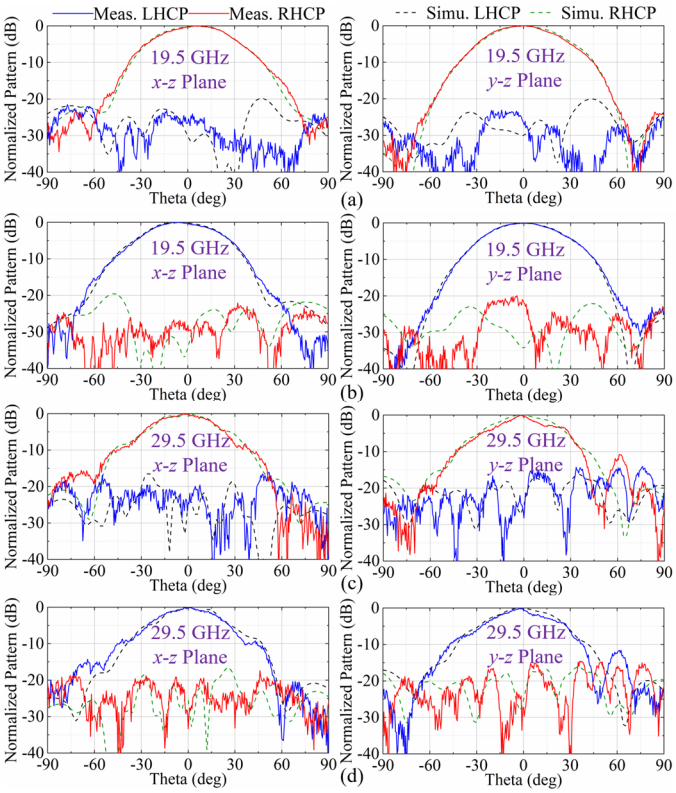

Fig. 9. Simulated and measured normalized radiation patterns at 19.5 GHz of *K*-band (a) RHCP and (b) LHCP arrays, and at 29.5 GHz of *Ka*-band (c) RHCP and (d) LHCP arrays.

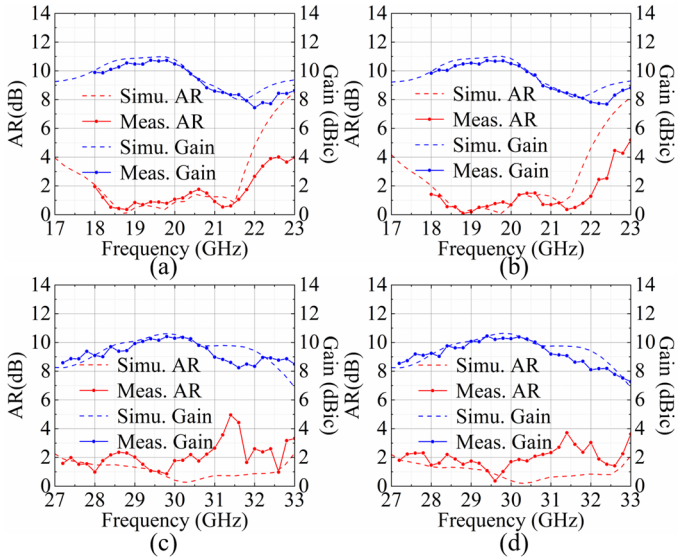

Fig. 10. Simulated and measured AR and peak gain values as a function of frequency of (a) *K*-band RHCP, (b) *K*-band LHCP, (c) *Ka*-band RHCP, and (d) *Ka*-band LHCP arrays.

B. Dual-Band Dual-CP TA Antenna Design

By utilizing the verified *K*- and *Ka*-band CP planar arrays as the feeding sources and properly distributing the dual-band 2 × 2 bit dual-CP cells on the TA aperture, an integrated dual-band dual-CP TA antenna with independently controllable beam directions is designed [see Fig. 1]. The TA panel occupies a quasi-circular area with a diameter of 216 mm, i.e., $14\lambda_K$, which contains 1268 *K*-band elements and 1201 *Ka*-band elements. The focal length is 151.2 mm, indicating an *F*/*D* ratio of 0.7 at both *K*- and *Ka*-bands for ensuring the oblique incident angles are no more than 36° at the edge of the TA.

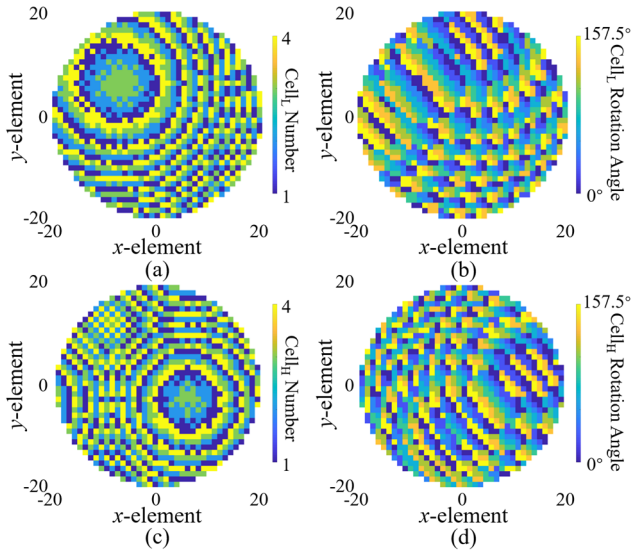

Fig. 11. Distributions of the *K*-band (a) element number and (b) element rotation angle, and *Ka*-band (c) element number and (d) element rotation angle of TA antenna across its radiating aperture.

The designed dual-band 2 × 2 bit dual-CP cells distributed on the TA aperture not only compensate for the optical path difference of the quasi-spherical waves radiated by the feeding sources, but also impose the required phase gradients for beam deflection [42], [43]. The element distribution and rotation angles are shown in Fig. 11. Consequently, the four generated highly-directive pencil beams are directing at (30°, 90°)/(-30°, 0°) for the *K*-band beams and at (20°, 0°)/(-20°, 90°) for the *Ka*-band beams [see Fig. 1]. Due to the large electrical size of the TA antenna, it would require an impractically huge amount of computational memory and time to perform full-wave simulations. Therefore, an efficient home-made code is employed for estimating the TA properties based on the vectorial near-field quantities, scattering parameters of the TA cells, and a near-field to far-field transform [38].

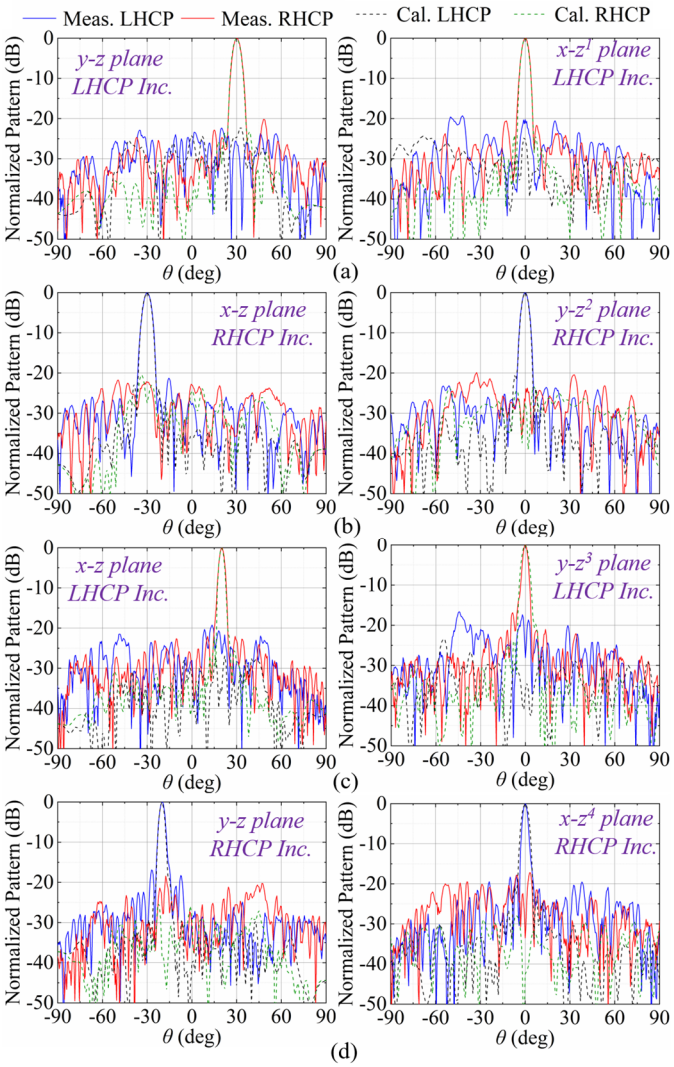

Fig. 12. Calculated and measured normalized CP radiation patterns of the TA antenna by exciting the *K*-band (a) LHCP and (b) RHCP feed arrays at 19.5 GHz, and the *Ka*-band (c) LHCP and (d) RHCP feed arrays at 29.5 GHz, where $\hat{z}^1 = \hat{z}cos30^o + \hat{y}sin30^o$, $\hat{z}^2 = \hat{z}cos30^o - \hat{x}sin30^o$, $\hat{z}^3 = \hat{z}cos20^o - \hat{y}sin20^o$, and $\hat{z}^4 = \hat{z}cos20^o + \hat{x}sin20^o$.

The calculated normalized radiation patterns of the TA antenna in the two orthogonal planes cutting through the main *K*- and *Ka*-band dual-CP beams are provided in Fig. 12. The four generated beams are all pointing to the targeted directions. The RHCP/LHCP beams at *K*-band possess calculated sidelobe levels (SLLs) and cross-polarization levels of -23.2/-24.9 dB and -20.5/-27.4 dB, respectively [see Fig. 12(a) and (b)]. Both of these two beams possess a calculated 2-dB gain and AR < 2 dB bandwidth of 12.3% [see Fig. 13(a) and (b)]. The calculated

peak gain values are both around 27.5 dBic for two CP beams at *K*-band, indicating an aperture efficiency of 29%. At *Ka*-band, the two CP beams own calculated SLLs and cross-polarization levels of -19.7/-36 dB and -20.8/-38.8 dB as reported in Fig. 12(c) and (d), respectively. The calculated 2-dB gain and AR < 2 dB bandwidths are 8.5% and 9.1% for the *Ka*-band CP beams [see Fig. 13(c) and (d)]. The calculated peak gain values are about 29.9 and 30.3 dBic at *Ka*-band, implying an aperture efficiency of 23.1% and 25.3% for the RHCP and LHCP beams, respectively. The detailed loss budgets at the operational bands are provided in Table II. The sum of all the losses is about 5.37 and 6.02 dB, indicating that the estimated aperture efficiencies are 29% and 25% at *K*- and *Ka*-bands, respectively. In future works, TA cells with lower insertion loss, a smaller TA cell size, and a finer phase resolution across the TA aperture will be investigated for improving the aperture efficiencies of such dual-band dual-CP TA antennas. It should be noted that feeding sources with a narrower beamwidth could be employed for further improving the aperture efficiency at the expense of an increased *F*/*D* ratio, thereby yielding a higher total profile. Other dual-band dual-CP TA antenna examples with beams pointing at large angles of about 45° off broadside have also been designed, showing that high-quality beams can still be obtained (not shown here for succinctness).

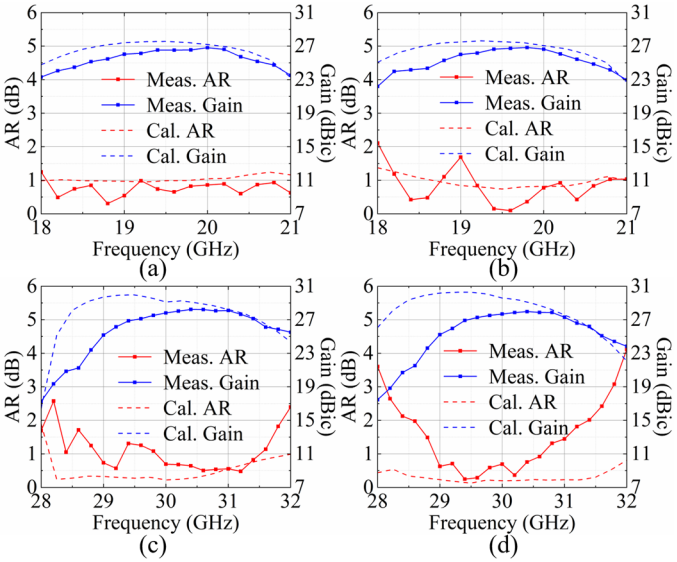

Fig. 13. Calculated and measured peak gain and AR values as a function of frequency for the dual-band dual-CP TA antenna excited by the (a) *K*-band LHCP, (b) *K*-band RHCP, (c) *Ka*-band LHCP, and (d) *Ka*-band RHCP planar feed arrays, respectively.

TABLE II. CALCULATED CONSTITUENTS OF APERTURE EFFICIENCY

Efficiency Type	*K*-band		*Ka*-band	
	Value (%)	Loss (dB)	Value (%)	Loss (dB)
Spillover Efficiency	75	1.25	79	1.02
Illumination Efficiency	95	0.22	87	0.61
Phase Quantization Efficiency	81	0.95	81	0.95
Cell Transmission Efficiency	78	1.1	78	1.06
Oblique incidence Efficiency	65	1.85	58	2.38
Total Aperture Efficiency	29	5.37	25	6.02

C. *Experimental Results*

The TA and the planar feeds are fabricated and integrated to construct the dual-band dual-CP TA antenna with the top and enlarged views of the *M1* and *M5* layers displayed in Fig. 14(a) and (b). The TA antenna is then measured in a far-field chamber for verifying the radiation performance [see Fig. 14(c)].

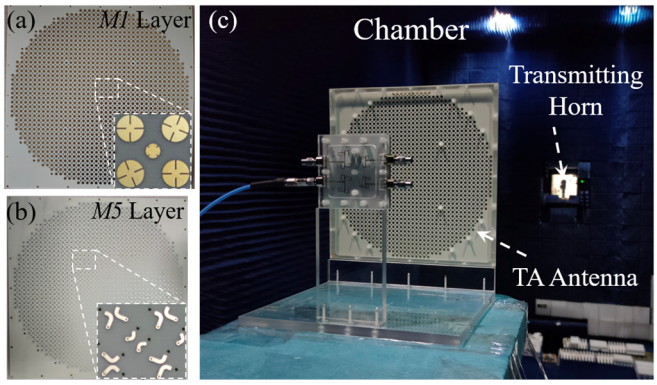

Fig. 14. Top and enlarged views of the (a) *M1* and (b) *M5* layers of the fabricated TA antenna. (c) Measurement environment of TA antenna in a far-field anechoic chamber.

The measured normalized CP radiation patterns of the TA antenna are provided in Fig. 12. The measured SLLs and cross-polarization levels are -20.2/-20.2 dB and -21.3/-22.2 dB for the CP beams at *K*-band, respectively [see Fig. 12(a) and (b)]. The measured 2-dB gain and AR bandwidths are 11.7% (18.5 – 20.8 GHz) and 10.2% (18.7 – 20.7 GHz), for both *K*-band CP beams, as shown in Fig. 13(a) and (b). The *K*-band beams both own measured peak gain and aperture efficiency of about 26.8 dBic and 24.6%, respectively. At *Ka*-band, the measured SLLs and cross-polarization levels are -16.9/-26.4 dB and -16.9/-25.8 dB for the CP beams, respectively [see Fig. 12(c) and (d)]. The measured 2-dB gain and AR < 2 dB bandwidths are 7.6% (29.3 – 31.6 GHz) and 7.3% (29.2 – 31.4 GHz) as reported in Fig. 13(c) and (d). The *Ka*-band RHCP and LHCP beams own measured peak gain values of 28.2 and 28.0 dBic, indicating that the aperture efficiencies are 15.6% and 14.9%. It can be seen from Fig. 13 that the measured operational bands shift slightly to higher frequencies by 1% at *K*-band and 2.7% at *Ka*-band. Considering such a frequency shift, the difference between the calculated and measured results are within an acceptable range. However, small discrepancies still exist and are attributed mainly to the following reasons: 1) the scattering parameters of the TA cells obtained using periodic unit cell simulations inevitably possess small deviations with those in a finate-sized TA due to the spatially interleaved arrangement of the *K*- and *Ka*-band elements, 2) inaccuracies introduced during the fabrication and assembly process, and 3) the slight curvature of the TA panel.

Table III presents a comparison between the proposed TA antenna and other previously reported dual-band or dual-CP TA antennas. It can be seen that the proposed TA antenna possesses a smaller TA panel thickness, a smaller *F*/*D* ratio, and a broader bandwidth. The designed TA antenna exhibits moderate aperture efficiencies when comparing with the reported dual-band or dual-CP TA antennas, all while possessing additional functionality and more degrees-of-freedom of beamforming. Most importantly, to the best of our knowledge, the demonstrated TA antenna is the first one that provides

TABLE III A COMPARISON AMONG DIFFERENT DUAL-BAND OR DUAL-CP TA ANTENNAS

	TA Features	Operating Frequency	TA Panel Thickness*	*F*/*D* Ratio	Element Spacing	Phase Compensation Technique**	Peak Gain (dBic)	Aperture Efficiency	2-dB Gain & AR < 2 dB Bandwidth
[7]	Dual-band	12 GHz / 14.2 GHz	1.62 mm ($0.06\lambda_L$)	0.65	11 mm ($0.44\lambda_L$ / $0.52\lambda_H$)	BP	23.2 / 23.6***	32.2% / 28.9%	7.2% / 4.6%
[13]	Dual-band	20 GHz / 30 GHz	7.5 mm ($0.5\lambda_L$)	0.69	5.3 mm ($0.35\lambda_L$ / $0.53\lambda_H$)	DP	15.3 / 15.3	10% / 6%	9.4% / 6.6%
[21]	Dual-CP	29 GHz	>13.2 mm (>$1.28\lambda_c$)	0.66	3.76 mm ($0.36\lambda_0$)	DP	30.2 / 30.2	23% / 23%	7.3% / 7.3%****
[22]	Dual-CP	20 GHz	1.61 mm ($0.11\lambda_c$)	0.85	7.5 mm ($0.5\lambda_0$)	DP + BP	22.3 / 22.5	27.6% / 24%	12.4% / 12.2%
This Work	Dual-band Dual-CP	19.5 GHz / 29.5 GHz	2.77 mm ($0.18\lambda_L$)	0.7	5.4 mm ($0.35\lambda_L$ / $0.53\lambda_H$)	DP + BP	26.8 / 26.8 28.2 / 28*****	24.6% / 24.6% 15.6% / 14.9%	11.7% / 10.2% 7.6% / 7.3%

* λ_L, λ_H, and λ_c denote the free-space wavelengths at low-band, high-band, and center frequency, respectively.
** DP represents dynamic phase compensation, while BP indicates Berry phase compensation.
*** The data before "/" is for low-band or RHCP beam values, and after "/" is for high-band or LHCP beam values.
**** The results are the 3-dB gain and AR < 3 dB bandwidth.

simultaneous dual-band and dual-CP beamforming characteristics.

IV. CONCLUSION

In conclusion, an integrated *K*- and *Ka*-band dual-CP TA antenna with independently controllable beam directions is designed, fabricated and experimented. The transmission coefficient matrix derivation of the proposed dual-CP cells is carried out initially. It reveals that polarization twisting TA cells possessing high cross-polarized and low co-polarized LP transmission characteristics can inherently provide highly-efficient CP transmission with handedness flip, along with advantages such as symmetrical structure, design simplification, and more consistent CP transmission magnitudes. In addition, planar *K*- and *Ka*-band RHCP/LHCP arrays are designed and functioned as the feeds for achieving low-profile characteristics. An integrated dual-band dual-CP TA antenna is designed and experimentally verified. The demonstrated dual-band dual-CP TA antenna can serve as a useful candidate for satellite communications, space applications, and so on.

V. ACKNOWLEDGMENT

The authors would like to thank T. Y. Huo for his help during the antenna fabrication and measurement.

REFERENCE

[1] W. Hong *et al*., "The Role of Millimeter-Wave Technologies in 5G/6G Wireless Communications," *IEEE J. Microw.*, vol. 1, no. 1, pp. 101-122, Jan. 2021.

[2] S. K. Rao, "Advanced antenna technologies for satellite communications payloads," *IEEE Trans. Antennas Propag.*, vol. 63, no. 4, pp. 1205-1217, Apr. 2015,

[3] H. Fenech, S. Amos, A. Tomatis, and V. Soumpholphakdy, "High throughput satellite systems: An analytical approach," *IEEE Trans. Aerosp. Elect. Syst.*, vol. 51, no. 1, pp. 192–202, Jan. 2015.

[4] L. Lei, J. Wan, and Q. Gong, "Multibeam antennas with reflector for high throughput satellite applications," *IEEE Aerosp. Electron. Syst. Mag.*, vol. 37, no. 2, pp. 34-46, Feb. 2022.

[5] J. R. Reis, M. Vala, and R. F. S. Caldeirinha, "Review paper on transmitarray antennas," *IEEE Access*, vol. 7, pp. 94171-94188, 2019.

[6] K. T. Pham, R. Sauleau, E. Fourn, F. Diaby, A. Clemente, and L. Dussopt, "Dual-band transmitarrays with dual-linear polarization at Ka-band," *IEEE Trans. Antennas Propag.*, vol. 65, no. 12, pp. 7009-7018, Dec. 2017.

[7] Y. -M. Cai *et al*., "Dual-band circularly polarized transmitarray with single linearly polarized feed," *IEEE Trans. Antennas Propag.*, vol. 68, no. 6, pp. 5015-5020, Jun. 2020.

[8] T. K. Pham, L. Guang, D. González-Ovejero, and R. Sauleau, "Dual-band transmitarray with low scan loss for satcom applications," *IEEE Trans. Antennas Propag.*, vol. 69, no. 3, pp. 1775-1780, Mar. 2021.

[9] L. H. He, Y. L. Ban, and G. Wu, "Dual-band quad-polarized transmitarray for 5G mm-wave application," *IEEE Access*, vol. 9, pp. 117520-117526, 2021.

[10] R. Y. Wu, Y. B. Li, W. Wu, C. B. Shi, and T. J. Cui, "High-gain dual-band transmitarray," *IEEE Trans. Antennas Propag.*, vol. 65, no. 7, pp. 3481-3488, July 2017.

[11] A. Aziz, F. Yang, S. Xu, and M. Li, "An efficient dual-band orthogonally polarized transmitarray design using three-dipole elements," *IEEE Antennas Wireless Propag. Lett.*, vol. 17, no. 2, pp. 319-322, Feb. 2018.

[12] A. Aziz, X. Zhang, F. Yang, S. Xu, and M. Li, "A dual-band orthogonally polarized contour beam transmitarray design," *IEEE Trans. Antennas Propag.*, vol. 69, no. 8, pp. 4538-4545, Aug. 2021.

[13] H. Hasani, J. S. Silva, S. Capdevila, M. García-Vigueras, and J. R. Mosig, "Dual-band circularly polarized transmitarray antenna for satellite communications at (20, 30) GHz," *IEEE Trans. Antennas Propag.*, vol. 67, no. 8, pp. 5325-5333, Aug. 2019.

[14] Z. Zhang, X. Li, C. Sun, Y. Liu, and G. Han, "Dual-band focused transmitarray antenna for microwave measurements," *IEEE Access*, vol. 8, pp. 100337-100345, 2020.

[15] M. Cai, Z. Yan, F. Fan, S. Yang, and X. Li, "Double-layer Ku/K dual-band orthogonally polarized high-efficiency transmitarray antenna," *IEEE Access*, vol. 9, pp. 89143-89149, 2021.

[16] D. Popovic and Z. Popovic, "Multibeam antennas with polarization and angle diversity," *IEEE Trans. Antennas Propag.*, vol. 50, no. 5, pp. 651-657, May 2002.

[17] F. Qin, S. Gao, W. -C. Cheng, Y. Liu, H. -L. Zhang, and G. Wei, "A high-gain transmitarray for generating dual-mode OAM beams," *IEEE Access*, vol. 6, pp. 61006-61013, 2018.

[18] K. Pham *et al*., "Design of wideband dual linearly polarized transmitarray antennas," *IEEE Trans. Antennas Propag.*, vol. 64, no. 5, pp. 2022-2026, May 2016.

[19] S. Li, Z. N. Chen, T. Li, F. H. Lin, and X. Yin, "Characterization of metasurface lens antenna for sub-6 GHz dual-polarization full-dimension massive MIMO and multibeam systems," *IEEE Trans. Antennas Propag.*, vol. 68, no. 3, pp. 1366-1377, Mar. 2020.

[20] X. Wang, Y. Cheng, and Y. Dong, "Millimeter-wave dual-polarized metal transmitarray antenna with wide gain bandwidth," *IEEE Antennas Wireless Propag. Lett.*, vol. 21, no. 2, pp. 381-385, Feb. 2022.

[21] K. T. Pham, A. Clemente, D. Blanco, and R. Sauleau, "Dual-circularly polarized high-gain transmitarray antennas at Ka-band," *IEEE Trans. Antennas Propag.*, vol. 68, no. 10, pp. 7223-7227, Oct. 2020.

[22] Z. H. Jiang, F. Wu, T. Yue, and W. Hong, "Wideband and low-profile integrated dual-circularly-polarized transmit-arrays enabled by antenna-filter-antenna phase shifting cells," *IEEE Trans. Antennas Propag.*, vol. 69, no. 11, pp. 7462-7475, Nov. 2021.

[23] D. Blanco and R. Sauleau, "Broadband and broad-angle multilayer polarizer based on hybrid optimization algorithm for low-cost Ka-band applications," *IEEE Trans. Antennas Propag.*, vol. 66, no. 4, pp. 1874-1881, Apr. 2018.

[24] Z. H. Jiang *et al.*, "A single noninterleaved metasurface for high-capacity and flexible mode multiplexing of higher-order Poincaré sphere beams," *Adv. Mater.*, vol. 32, no. 6, Feb. 2020.

[25] Y. Couble, C. Rosenberg, E. Chaput, J. Dupé, C. Baudoin, and A. Beylot, "Two-color scheme for a multi-beam satellite return link: impact of interference coordination," *IEEE J. Sel. Areas Commun.,* vol. 36, no. 5, pp. 993-1003, May 2018.

[26] Q. Luo *et al*., "Multibeam dual-circularly polarized reflectarray for connected and autonomous vehicles," *IEEE Trans. Veh. Technol.*, vol. 68, no. 4, pp. 3574-3585, Apr. 2019.

[27] X. Tong, Z. H. Jiang, Y. Li, F. Wu, R. Sauleau, and W. Hong, "Dual-wideband dual-circularly-polarized shared-aperture reflectarrays with a single functional substrate for K-/Ka-Band applications," *IEEE Trans. Antennas Propag.*, doi: 10.1109/TAP.2022.3145484

[28] P. Naseri, M. Riel, Y. Demers, and S. V. Hum, "A dual-band dual-circularly polarized reflectarray for K/Ka-band space applications," *IEEE Trans. Antennas Propag.*, vol. 68, no. 6, pp. 4627-4637, Jun. 2020.

[29] P. Xu, L. Li, R. Li, and H. Liu, "Dual-circularly polarized spin-decoupled reflectarray with FSS-back for independent operating at Ku/Ka-band," *IEEE Trans. Antennas Propag.*, vol. 69, no. 10, pp. 7041-7046, Oct. 2021.

[30] M. O. Bagheri, H. R. Hassani, and B. Rahmati, "Dual-band, dual-polarised metallic slot transmitarray antenna," *IET Microw., Antennas Propag.*, vol. 11, pp. 402–409, 2017.

[31] A. Aziz, F. Yang, S. Xu, M. Li, and H. -T. Chen, "A high-gain dual-band and dual-polarized transmitarray using novel loop elements," *IEEE Antennas Wireless Propag. Lett.*, vol. 18, no. 6, pp. 1213-1217, Jun. 2019.

[32] R. H. Phillion, and M. Okoniewski, "Lenses for circular polarization using planar arrays of rotated passive elements," *IEEE Trans. Antennas Propag.*, vol. 59, no. 4, pp. 1217-1227, Apr. 2011.

[33] P. Naseri, S. A. Matos, J. R. Costa, and C. A. Fernandes, "Phase-delay versus phase-rotation cells for circular polarization transmit arrays—application to satellite Ka-band beam steering," *IEEE Trans. Antennas Propag.*, vol. 66, no. 3, pp. 1236-1247, March 2018.

[34] Z. H. Jiang, M. D. Gregory, and D. H. Werner, "Broadband high directivity multibeam emission through transformation optics-enabled metamaterial lenses," *IEEE Trans. Antennas Propag.*, vol. 60, no. 11, pp. 5063-5074, Nov. 2012.

[35] M. Selvanayagam and G. V. Eleftheriades, "Design and measurement of tensor impedance transmitarrays for chiral polarization control," *IEEE Trans. Microw. Theory Techn.*, vol. 64, no. 2, pp. 414-428, Feb. 2016.

[36] Y. He and Y. Li, "Dual-polarized microstrip antennas with capacitive via fence for wide beamwidth and high isolation," *IEEE Trans. Antennas Propag.*, vol. 68, no. 7, pp. 5095-5103, Jul. 2020.

[37] J. Huang and R. J. Pogorzelski, "A Ka-band microstrip reflectarray with elements having variable rotation angles," *IEEE Trans. Antennas Propag.*, vol. 46, no. 5, pp. 650-656, May 1998.

[38] Z. H. Jiang, L. Kang, T. Yue, W. Hong, and D. H. Werner, "Wideband transmit arrays based on anisotropic impedance surfaces for circularly polarized single-feed multibeam generation in the Q-band," *IEEE Trans. Antennas Propag.*, vol. 68, no. 1, pp. 217-229, Jan. 2020.

[39] Z. H. Jiang, Y. Zhang, J. Xu, Y. Yu, and W. Hong, "Integrated broadband circularly polarized multibeam antennas using Berry-phase transmit-arrays for Ka-band applications," *IEEE Trans. Antennas Propag.*, vol. 68, no. 2, pp. 859-872, Feb. 2020.

[40] A. Bhattacharyya, O. Fordham, and Y. Liu, "Analysis of stripline-fed slot-coupled patch antennas with vias for parallel-plate mode suppression," *IEEE Trans. Antennas Propag.*, vol. 46, no. 4, pp. 538–545, Apr. 1998.

[41] Z. H. Jiang, L. Kang, W. Hong, and D. H. Werner, "Highly efficient broadband multiplexed millimeter-wave vortices from metasurface-enabled transmit-arrays of subwavelength thickness," *Phys. Rev. Appl.*, vol. 9, no. 6, Jun. 2018, Art. no. 064009

[42] Z. H. Jiang, T. Yue, and W. Hong, "Low-profile and wideband dual-circularly polarized reflect-arrays based on rotated metal-backed dual-polarized aperture-coupled patch elements," *IEEE Trans. Antennas Propag.*, vol. 68, no. 3, pp. 2108-2117, Mar. 2020.

[43] A. H. Abdelrahman, F. Yang, A. Z. Elsherbeni, P. Nayeri, and C. A. Balanis, *Analysis and Design of Transmitarray Antennas*. San Francisco, CA, USA: Morgan & Claypool, 2017.

Xuanfeng Tong (S'20) was born in Taizhou, Jiangsu, China, in 1993. He received the B.S. degree from Chifeng University, Chifeng, China, in 2016, and the M.S. degree from the School of Electronic Information, Soochow University, Suzhou, China, in 2019. He is currently pursing the Ph.D degree with Southeast University, Nanjing, China.

His main research interests include dual-band and dual-polarized antenna, reflectarray and transmitarray.

Mr. Tong was a recipient of the 2018 Nation Scholarship for Graduate Students and the Best Student Paper Award at the 2021 IEEE International Workshop on Electromagnetics (iWEM), Guangzhou, China.

Zhi Hao Jiang (S'07–M'13) was born in Nanjing, China, in 1986. He received the B.S. degree in radio engineering from Southeast University, Nanjing, in 2008, and the Ph.D. degree in electrical engineering from The Pennsylvania State University, University Park, State College, PA, USA, in 2013. From 2013 to 2016, he was a Post-Doctoral Fellow with the Computational Electromagnetics and Antennas Research Laboratory, Department of Electrical Engineering, The Pennsylvania State University. He is currently a Professor with the State Key Laboratory of Millimeter Waves, School of Information Science and Engineering, Southeast University.

Dr. Jiang has authored or co-authored more than 100 papers in peer-reviewed journals, over 70 papers in conference proceedings, as well as 9 book chapters. He has also co-edited two books: *Electromagnetic Vortices: Wave Phenomena and Engineering Applications* (Wiley/IEEE Press, 2021), *Electromagnetics of Body-Area Networks: Antennas, Propagation, and RF Systems* (Wiley/IEEE Press, 2016). He holds 7 granted U.S. patents and 15 granted Chinese patents. He has served as the TPC Co-Chair or a TPC Member for multiple international conferences. He was a recipient of the Outstanding Youth Scholar of National Science Foundation of China in 2021, the IEEE Microwave Prize in 2021, the Young Scientist Award at the URSI-GASS in 2020, the Young Scientist Award at the 2019 ACES-China Conference, the High-Level Innovative and Entrepreneurial Talent presented by Jiangsu Province, China, in 2017, the Thousands of Young Talents presented by China government in 2016, the 2012 A. J. Ferraro Outstanding Doctoral Research Award in Electromagnetics, and several best (student) paper awards at international conferences. He is a Senior Member of CIE, serves as the Associate Editor of *IET Communications*, was a Guest Editor of *International Journal of RF and Microwave Computer-Aided Engineering*. His current research interests include microwave/millimeter-wave antennas and circuits, millimeter-wave systems, impedance surfaces, metamaterials, and analytical methods.

Yuan Li (S'21) was born in Huainan, Anhui, China, in 1994. He received the B.S. degree from University of Electronic Science and Technology of China (UESTC), Chengdu, China, in 2017. He is currently pursing the Ph.D degree with Southeast University, Nanjing, China.

His main research interests include circular polarization selective surface, metasurface, reflectarray and transmitarray.

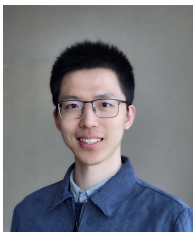

Fan Wu (S'15–M'18) was born in Jiangxi, China. He received the B.Eng and M.Eng degrees in electronic engineering from Beijing Jiaotong University, Beijing, China, in 2012 and 2015, respectively, and the Ph.D. degree in electronic engineering from City University of Hong Kong, Hong Kong, in 2018.

He is currently an Assistant Professor with the State Key Laboratory of Millimeter Waves, School of Information Science and Engineering, Southeast University, Nanjing, China. His current research is in the areas of space-fed antennas, circularly-polarized wideband antennas and reconfigurable antenna designs.

Dr. Wu was a recipient of the Honorable Mention at the student contest of the 2018 IEEE APS-URSI Conference and Exhibition held in Boston, USA. He served as a regular reviewer for numerous peer-reviewed international journals including the IEEE T-AP and AWPL.

Jianjun Wu was born in Shanghai, China, in 1978. He received the B.S. degree in communication engineering from Xi'an University of Electronic Science and Technology in 2002, and the MA.Eng degree in electromagnetic field and microwave technology from Xi'an University of Electronic Science and Technology in 2005. Since 2005, he has worked in ZTE Corporation. He is now a senior wireless system engineer and a technical researcher in the State Key Laboratory of Mobile Network and Mobile Multimedia Technology.

Since taking office, Mr. Wu has participated in several national and company-level major projects, and has published articles in academic conferences and Top journals at home and abroad for many times. He has more than 10 granted Chinese patents, and the Pre5G Massive MIMO developed by him has won the "Best Mobile Technology Breakthrough Award" of the Global Mobile Awards of the Barcelona Exhibition, which is currently recognized by the industry as the highest award and the "CTO Choice Award". The dynamic RIS (Reconfigurable Intelligence Surface) developed was also the shortlist of "Mobile Technology Breakthrough Award" of Barcelona Exhibition for 23 years, and has won the excellent project manager of ZTE for many times and served as a researcher in key laboratories. His current research interests include: mobile communication RF technology, microwave/millimeter wave multi-antenna technology, Massive MIMO base station, RIS, and ISAC (Integrated Sensing And Communication).

Ronan Sauleau (M'04–SM'06–F'18) graduated in electrical engineering and radio communications from the Institut National des Sciences Appliquées, Rennes, France, in 1995. He received the Agrégation degree from the Ecole Normale Supérieure de Cachan, France, in 1996, and the Doctoral degree in signal processing and telecommunications and the "Habilitation à Diriger des Recherches" degree, both from the University of Rennes 1, France, in 1999 and 2005, respectively. He was an Assistant Professor and Associate Professor at the University of Rennes 1, between September 2000 and November 2005, and between December 2005 and October 2009, respectively. He has been appointed as a full Professor in the same University since November 2009. His current research fields are numerical modeling, millimeter-wave beam steering antennas, substrate integrated waveguide antennas, lens-based focusing devices, periodic and non-periodic structures (frequency selective surface (FSS), metasurfaces, polarizers, reflectarrays, and transmitarrays) and biological effects of millimeter waves.

He has been involved in more than 70 research projects at the national and European levels and has co-supervised 27 post-doctoral fellows, 57 PhD students and 50 master students.

He has received 20 patents and is the author or coauthor of more than 275 journal papers and 570 publications in international conferences and workshops. He was co-director of the research Department 'Antenna and Microwave Devices' at IETR and deputy director of IETR between 2012 and 2016. He is now director of IETR. Prof. Sauleau received the 2004 ISAP Conference Young Researcher Scientist Fellowship (Japan) and the first Young Researcher Prize in Brittany, France, in 2001 for his research work on gain-enhanced Fabry-Perot antennas. In September 2007, he was elevated to Junior member of the "Institut Universitaire de France". He was awarded the Bronze medal by Centre National de la Recherche Scientifique (CNRS) in 2008, and the silver medal in 2020. He received the 2021 Antenna EurAAP Award. He was the co-recipient of several international conference awards with some of his students (International School of Bioelectromagnetics 2005, Bioelectromagnetics Society (BEMS)'2006, Microwaves, Radar and Remote Sensing Symposium (MRRS)'2008, European Materials Research Society (E-MRS)'2011, BEMS'2011, International Microwave Symposium (IMS)'2012, Antenna Technology and Applied Electromagnetics (Antem)'2012, Bioelec-tromagnetics (BioEM)'2015, European Conference on Antennas and Propa-gation (EuCAP)'2019, and EuCAP'2021). He served as a guest editor for the IEEE Antennas Propogat. Special Issue on "Antennas and Propagation at mm and sub mm waves". He has served as a national delegate for several National Delegate for several European Cooperation in Science and Technology (EU

COST) actions. He has served as a national delegate for European School of Antennas and Propagation (EurAAP) and as a member of the board of Director of EurAAP from 2013 to 2018.

Wei Hong (M'92–SM'07–F'12) received the B.S. degree from the University of Information Engineering, Zhengzhou, China, in 1982, and the M.S. and Ph.D. degrees from Southeast University, Nanjing, China, in 1985 and 1988, respectively, all in radio engineering.

He has been with the State Key Laboratory of Millimeter Waves, Southeast University, since 1988, where he has also been the Director of the Laboratory since 2003. He is currently a Professor of the School of Information Science and Engineering with Southeast University. In 1993 and 1995–1998, he was a short-term Visiting Scholar with the University of California at Berkeley and at Santa Cruz, CA, USA, respectively. He has authored or co-authored over 300 technical publications and authored two books. His current research interests include numerical methods for electromagnetic problems, millimeter-wave theory and technology, antennas, electromagnetic scattering, and RF technology for mobile communications

Dr. Hong was an Elected IEEE MTT-S AdCom Member during 2014–2016. He is a fellow of IEEE and Chinese Institute of Electronics (CIE). He twice awarded the National Natural Prizes, and thrice awarded the first-class Science and Technology Progress Prizes issued by the Ministry of Education of China and Jiangsu Province Government. Besides, he also received the Foundations for China Distinguished Young Investigators and for "Innovation Group" issued by the NSF of China. He is the Vice President of the CIE Microwave Society and Antenna Society and the Chair of the IEEE MTTS/APS/EMCS Joint Nanjing Chapter. He served as the Associate Editor of the IEEE TRANSACTIONS ON MICROWAVE THEORY AND TECHNIQUES from 2007 to 2010, and one of the Guest Editors for the 5G special issue of the IEEE TRANSACTIONS ON ANTENNAS AND PROPAGATION in 2017.